AGU PUBLICATIONS

JGR

Journal of Geophysical Research: Atmospheres

RESEARCH ARTICLE
10.1002/2016JD025616

Key Points:
- Model results indicate that there is a preferred location of vertical transport from the boundary layer to UTLS
- Subseasonal-scale dynamics of the Asian monsoon anticyclone is an important driver of UTLS chemical transport
- The season's slow ascent in residual circulation limits the efficiency of vertical transport into the stratosphere from the ASM

Supporting Information:
- Supporting Information S1
- Movie S1

Correspondence to:
L. L. Pan,
liwen@ucar.edu

Citation:
Pan, L. L., S. B. Honomichl, D. E. Kinnison, M. Abalos, W. J. Randel, J. W. Bergman, and J. Bian (2016), Transport of chemical tracers from the boundary layer to stratosphere associated with the dynamics of the Asian summer monsoon, *J. Geophys. Res. Atmos.*, *121*, doi:10.1002/2016JD025616.

Received 5 JUL 2016
Accepted 9 NOV 2016
Accepted article online 15 NOV 2016

Transport of chemical tracers from the boundary layer to stratosphere associated with the dynamics of the Asian summer monsoon

Laura L. Pan[1], Shawn B. Honomichl[1], Douglas E. Kinnison[1], Marta Abalos[1], William J. Randel[1], John W. Bergman[2,1], and Jianchun Bian[3]

[1]National Center for Atmospheric Research, Boulder, Colorado, USA, [2]Bay Area Environmental Research Institute, Sonoma, California, USA, [3]Key Laboratory of Middle Atmospheric and Global Environment Observation, Institute of Atmospheric Physics, Chinese Academy of Science, Beijing, China

Abstract Chemical transport associated with the dynamics of the Asian summer monsoon (ASM) system is investigated using model output from the National Center for Atmospheric Research (NCAR) Whole Atmosphere Community Climate Model run in specified dynamics mode. The 3-D day-to-day behavior of modeled carbon monoxide is analyzed together with dynamical fields and transport boundaries to identify preferred locations of uplifting from the boundary layer, the role of subseasonal-scale dynamics in the upper troposphere and lower stratosphere (UTLS), and the relationship of ASM transport and the stratospheric residual circulation. The model simulation of CO shows the intraseasonal east-west oscillation of the anticyclone may play an essential role in transporting convectively pumped boundary layer pollutants in the UTLS. A statistical analysis of 11 year CO also shows that the southern flank of the Tibetan plateau is a preferred location for boundary layer tracers to be lofted to the tropopause region. The vertical structure of a model tracer (E90) further shows that the rapid ASM vertical transport is only effective up to the tropopause level (around 400 K). The efficiency of continued vertical transport into the deep stratosphere is limited by the slow ascent associated with the zonal-mean residual circulation in the lower stratosphere during northern summer. Quasi-isentropic transport near the 400 K potential temperature level is likely the most effective process for ASM anticyclone air to enter the stratosphere.

1. Introduction

From a global dynamics perspective, the Asian summer monsoon (ASM) is a dominant system in the boreal summer season [e.g., *Hoskins and Rodwell*, 1995]. From the chemical composition and transport perspective, monsoon convection coupled with the strong local emission sources of South and Southeast Asia produces a significant anthropogenic signature on the chemical composition at the upper troposphere and lower stratosphere (UTLS) [*Randel and Park*, 2006; *Park et al*., 2007; *Randel et al*., 2010]. The ASM region is also found to have a persistent aerosol layer near the tropopause [*Vernier et al*., 2011; *Thomason and Vernier*, 2013] that is likely caused by convective uplifting of anthropogenic precursors [*Vernier et al*., 2015; *Yu et al*., 2015]. However, the radiative impacts of water vapor and aerosols associated with ASM convection are yet to be fully quantified. Considering the potential impacts from the complex and increasing emissions from the source region due to the rapid economic development in Asia, an accurate representation of the ASM transport process in global chemistry-climate models is important.

Satellite data highlight the significant chemical signature in the UTLS on the seasonal scale, but the data are limited by sampling and do not resolve day-to-day variability necessary for process studies. Targeted in situ measurements are necessary for resolving details needed to address process level questions, such as what are the most impactful source regions, what is the chemical and aerosol content of the ASM UTLS, what is the time scale and depth of convective uplifting, how is the monsoon transport connected to the large-scale circulation, and what are the subsequent impacts on stratospheric chemistry? Opportunities for obtaining in situ measurements, especially airborne studies, have been limited due to operational difficulties in the region. The primary goal of this work is to examine the 3-D day-to-day behavior of the tracer transport in the ASM using a state-of-art chemistry-climate model (CCM) to identify a set of key transport questions that can potentially be targeted by airborne campaigns.

Multiyear output of NCAR Whole Atmosphere Community Climate Model V4 from a specified dynamics (WACCM4-SD) run is used in this work to examine the relationships between chemical tracers, the dynamical variables and transport boundaries, and to investigate the role of subseasonal-scale dynamics for upper troposphere (UT) composition. Our analyses focus on the following interrelated questions:

1. Does the transport of the ASM follow a "chimney" model; i.e., transport behaves more or less as a stationary system, venting pollutants vertically into the stratosphere, as is often implied by the satellite seasonal climatology? Or is the system more like a migrating "blower"; i.e., it distributes the pollutants both vertically and quasi-horizontally at the UTLS level?
2. Are there preferred locations of uplifting?
3. What is the relationship of ASM transport with the stratospheric large-scale Brewer-Dobson circulation?

We choose carbon monoxide (CO) as a boundary layer tracer for transport diagnosis. CO is a representative pollution tracer and is retrieved by a number of satellite instruments. Satellite data analyses have also shown that a suite of boundary layer tracers with observed UT enhancement in the ASM anticyclone are well-correlated with CO [*Park et al*., 2008]. The surface emission of CO, however, has a seasonal variation tied to biomass burning and additional human activities. When focusing on the ASM impact on the stratosphere, we also utilize a model tracer E90 and additional vertical wind analyses; details are provided in section 6. We often simply refer to both CO and E90 as "tracers" in the discussion.

This work is complementary to an increasing number of Lagrangian model studies of Asian monsoon transport [e.g., *Chen et al*., 2012; *Bergman et al*., 2013; *Garny and Randel*, 2016], where the origins and fates of air masses within the Asian monsoon anticyclone are statistically analyzed using idealized air parcels and their trajectories. Ensemble trajectory analysis is a powerful tool, and the studies have provided many useful insights. The primary weakness of these calculations stems from their dependence on analyzed wind fields; in this context, vertical transport due to (unresolved) convection is particularly uncertain. Trajectory calculations also do not have the ability to represent chemical content nor its change due to mixing and dilution during transport. Recent work using the Chemical Lagrangian Model of the Stratosphere (CLaMS) begins to address some of these issues [*Vogel et al*., 2015]. Analyses of tracers from CCMs will provide complementary perspectives on these challenging issues.

An adequate representation of ASM transport in CCMs is important and needs to be evaluated with observations. The analysis and conclusions presented in this study not only provide a set of hypotheses for designing sampling strategies in airborne studies and other ground based in situ measurements but also explore potential diagnostics for evaluating the representation of ASM processes in CCMs.

2. WACCM Model and the Specified Dynamics (SD) Run

The Whole-Atmosphere Community Climate Model, version 4 (WACCM4) [*Marsh et al*., 2013], developed at the National Center for Atmospheric Research (NCAR), includes the physical parameterizations and finite volume dynamical core [*Lin*, 2004] from the Community Atmosphere Model, version 4 [*Neale et al*., 2013]. The convection is parameterized using the Zhang-McFarlane scheme [*Zhang and McFarlane*, 1995] for deep convection and the Hack scheme [*Hack*, 1994] for shallow convection. The model domain extends from the Earth's surface to the lower thermosphere (140 km). For the simulation used in this study, the model uses a regular 2.5°×1.9° longitude-latitude grid, with 88 vertical levels on a hybrid-pressure vertical grid. For pressures $<$ 100 hPa, the vertical coordinate is isobaric; at higher pressures the coordinate is terrain following. The resolution in the UTLS is ~1 km.

The chemical module of WACCM4 is based upon the 3-D chemical transport Model of OZone and Related Tracers, version 3 [*Kinnison et al*., 2007]. This module includes a detailed representation of the chemical and physical processes in the troposphere through the lower thermosphere. The species included within this mechanism are contained within the O_x, NO_x, HO_x, ClO_x, and BrO_x chemical families, along with CH_4 and its degradation products. In addition, 14 primary nonmethane hydrocarbons and related oxygenated organic compounds are represented along with their surface emissions [*Emmons et al*., 2010]. Primary anthropogenic, biogenic, and ocean emissions for CO in this study are taken from Precursors of Ozone and their Effects in the Troposphere database [*Granier et al*., 2005; *Olivier et al*., 2003]. Biomass burning CO emissions are taken from Global Fire Emissions Database, version 2, which is currently available for 1997–2007 [*van der Werf et al*.,

2006]. This chemical mechanism contains 122 species, >220 gas-phase reactions, 71 photoclytic processes, and 17 heterogeneous reactions on multiple aerosol types.

In this study, "specified dynamics" run of WACCM4 is used, in which the model is "nudged" using external meteorological fields [*Kunz et al*., 2011; *Lamarque et al*., 2012]. These meteorological fields come from the NASA Global Modeling and Assimilation Office Goddard Earth Observing System Model, version 5 [*Rienecker et al*., 2008]. At each model time step (every 30 min), a nudging factor of 0.01 is applied to the horizontal wind and temperature fields up to an altitude of ~50 km, resulting in dynamical fields that are consistent with GOES 5 [*Kunz et al*., 2011]. The main effect of nudging is to provide meteorological conditions for WACCM4 chemistry that are consistent with analyzed winds and temperature, allowing comparisons between WACCM4 and observed chemical distributions. The nudging does not directly change the convection parameterization in the model, although it will influence the representation of convection. The impacts of nudging on model transport, especially the vertical transport, are not yet characterized. The analysis presented here is primarily based on CO mixing ratios from 11 years (2000–2010) of WACCM4-SD with supplementary analysis of the idealized model tracer E90 [*Prather et al*., 2011] from an additional 1 year (2014) output.

The WACCM4-SD model representation of UTLS tracers has been compared with Atmospheric Chemistry Experiment-Fourier transform spectrometer and Microwave Limb Sounder (MLS) satellite data [*Park et al*., 2013]. These comparisons show that the model reliably simulates the large-scale distributions of CO, C_2H_6, C_2H_2, and HCN in the UTLS. Quantitatively, WACCM4-SD CO mixing ratio shows an approximately 10% high bias during the ASM season in 15°–30°N latitude band compared with MLS 147 hPa monthly zonal mean. Although not shown, we have also examined the model representation of the ASM by comparing the June–August (JJA) seasonal means of CO from the model to values from MLS at 100 and 150 hPa levels. This comparison demonstrates that the modeled CO enhancements in this region are well collocated with satellite data for all years we examined (2005–2010).

3. UTLS Tracer Structure With Respect to the Transport Boundaries

The dynamical structure of the ASM UTLS is characterized by an anticyclonic flow pattern associated with the Tibetan High [*Krishnamurti and Bhalme*, 1976]. Satellite data show that the anticyclone has a pronounced chemical signature with enhanced tropospheric sourced trace gas species, such as water vapor, carbon monoxide, and other pollution and biomass burning tracers, such as HCN [*Randel and Park*, 2006; *Park et al*., 2007, 2008; *Randel et al*., 2010]. These observations demonstrate that the ASM provides a significant transport pathway for surface emission to enter the UTLS.

Using the WACCM4-SD CO as a pollution tracer, we examine the relationship of tracer enhancement with the tropopause and the boundary of the anticyclone. Figures 1a and 1b shows 11 year (2000–2010) JJA seasonal mean tropopause height and tropopause potential temperature (θ) from the National Centers for Environmental Prediction final analyses of the Global Forecast System (GFS) [*National Centers for Environmental Prediction/National Weather Service/NOAA/U.S. Department of Commerce*, 2000]. The tropopause here is based on the World Meteorological Organization (WMO) lapse rate definition [*World Meteorological Organization*, 1957] and is provided in the GFS data set. We also included JJA cold point tropopause height (Figure 1c) based on 4 years of Constellation Observing System for Meteorology, Ionosphere, and Climate (COSMIC) satellite GPS data analyses [*Munchak and Pan*, 2014]. It is important to note that the cold point is only meaningful as a tropopause definition in the tropics, because it is no longer an air mass boundary outside the tropics [*Munchak and Pan et al*., 2014]. The result shown in Figure 1c is derived from profiles within the tropical regime. We filtered out the extratropical influence by choosing only profiles with the WMO tropopause altitude higher than 14.5 km.

In the JJA season, the ASM region has the globally highest tropopause altitude. The high tropopause is a balanced dynamical structure tied to the strong anticyclonic circulation of the ASM [e.g., *Hoskins et al*., 1985]. Both the tropopause height and potential temperature of the ASM region are higher than that of the equatorial tropics, consistent with the analyses of *Highwood and Hoskins* [1998] and *Dethof et al*. [1999]. As shown in Figure 1, the ASM anticyclone region is the only region where the seasonal mean tropopause height is higher than 16.5 km; values greater than 16.7 km correspond to tropopause pressures of 100 hPa or lower. In terms of potential temperature (θ), the ASM tropopause has values exceeding 380 K, while the equatorial tropical tropopause θ is generally 370–375 K for the season. Note that the region of high

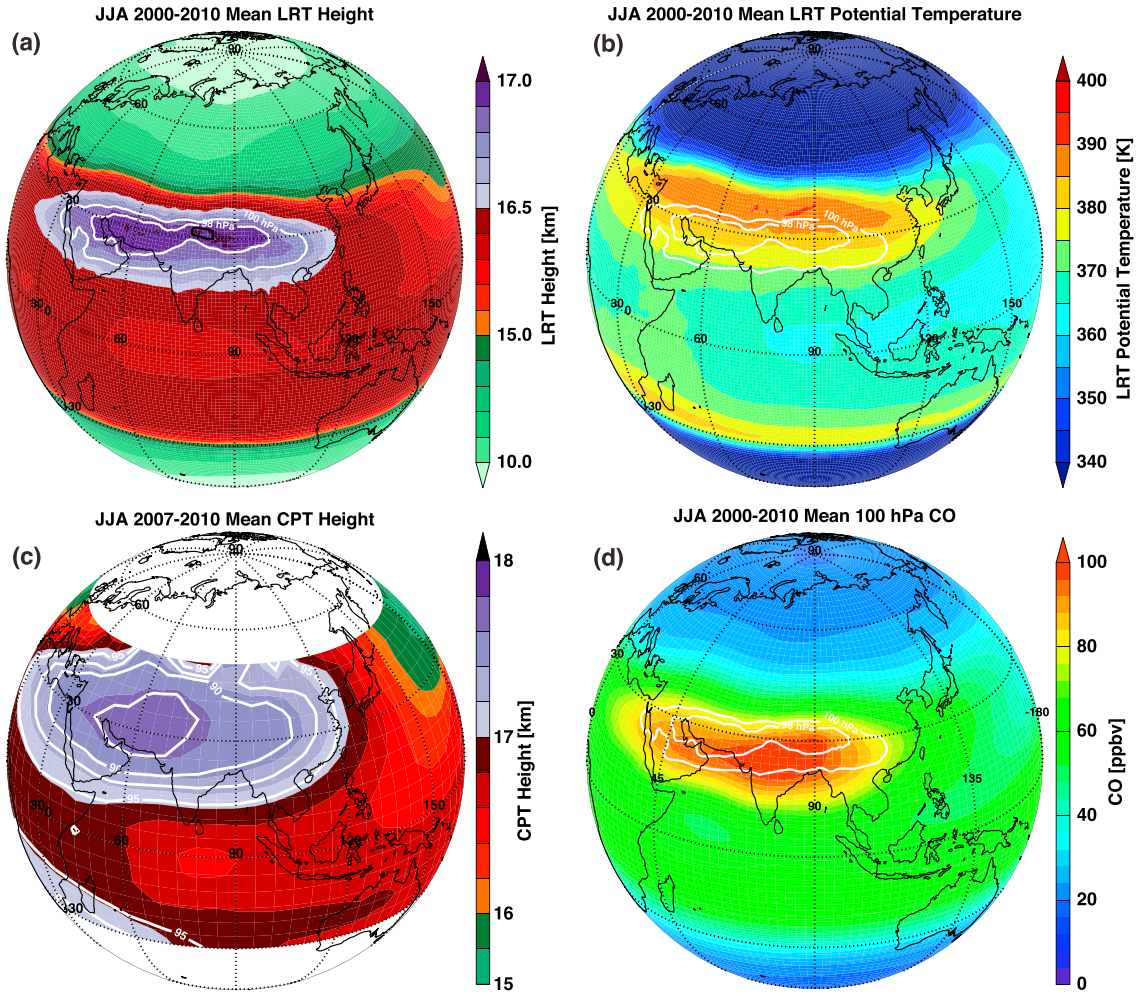

Figure 1. June–August mean (a) lapse rate tropopause (LRT) height (km) from GFS analyses, (b) LRT potential temperature (K) also from GFS, (c) cold point tropopause (CPT) height (km) from COSMIC GPS data, and (d) CO mixing ratio (ppbv) at 100 hPa from WACCM. LRT pressure is shown in Figures 1a, 1b, and 1d (100 and 95 hPa, white contours). Selected levels of CPT pressure from COSMIC are shown in Figure 1c (87.5, 90, 92.5, and 95 hPa, white contours).

tropopause θ is north of the highest tropopause height, which reflects the inclining θ surface at the edge of the tropics near the subtropical jet. The cold point tropopause in the center of the seasonal mean feature is approximately 18 km, about a kilometer higher than the lapse rate tropopause.

Figure 1d shows the 11 year JJA mean CO at 100 hPa from WACCM4-SD. Comparing the tropopause structure with the CO field, it is clear that the enhanced chemical signature at 100 hPa is associated with the ASM region's bulging tropopause. This implies that the high values of CO there could result from the fact that air at the 100 hPa is tropospheric within the ASM tropospheric "bubble" and is stratospheric outside.

The bulging structure and the higher potential temperature of the ASM tropopause present a unique isentropic transport pathway into the stratosphere, including the equatorial lower stratosphere, for the air mass inside the anticyclone. The elevated cold point tropopause (CPT) in the ASM region also allows moist air to bypass the local cold point before entering the stratosphere, as pointed out in *Dethof et al.* [1999].

The relationship of tracer and dynamical boundaries is next examined in the daily CO behavior. Figure 2 shows an example of a 3-D view of CO and associated dynamical variables for a selected day (22 August 2005), a day of strong uplifting that is reflected in the CO field. The latitude-height and longitude-height cross sections across the "center" of the anticyclone, identified by the maximum geopotential height (GPH), and the plane view at 100 hPa provide a near-instantaneous 3-D view of the chemical structure associated with the ASM anticyclone.

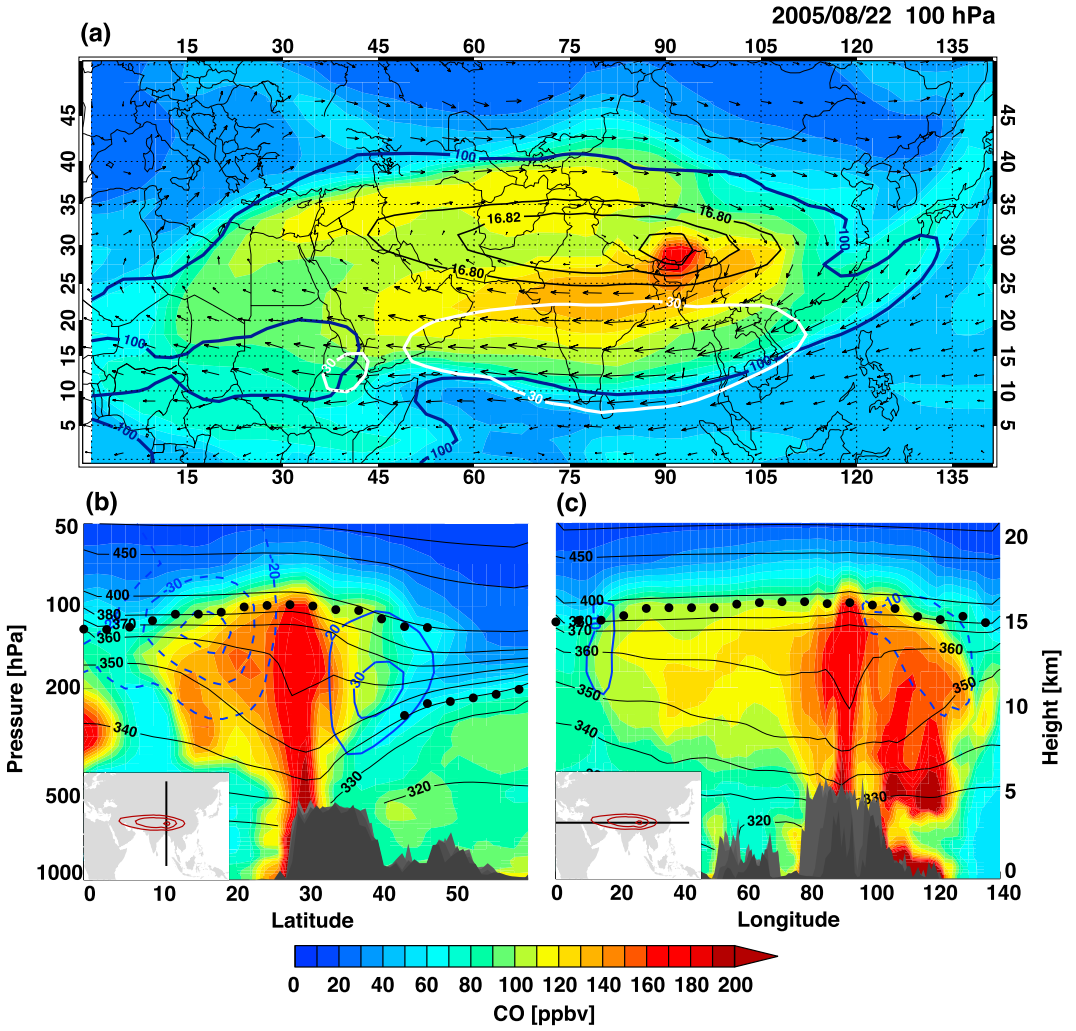

Figure 2. CO mixing ratio (ppbv) distribution from WACCM4-SD on 22 August 2005. (a) CO at 100 hPa (color shading) with horizontal wind (arrows); selected GPH (thin black contours); 100 hPa tropopause (blue contour), i.e., the interception of the tropopause with the 100 hPa pressure surface; and easterly jet location indicated by the 30 m/s zonal wind (white contour). (b) Latitude-pressure/altitude cross section of CO (ppbv) along 90 E (as shown on the locator map at the lower corner). Also shown are the tropopause height (black dots), selected isentropes (K; thin black lines), and locations of the easterly and westerly jets as indicated by selected zonal wind contours (m/s; blue dash and solid, respectively). (c) Same as Figure 2b but for longitude-pressure/altitude cross section.

The 100 hPa plane view shows a picture consistent with the seasonal climatology (Figure 1d) that the CO enhancement is largely contained within the "tropospheric bubble." The intersection of the tropopause with the 100 hPa pressure surface generally marks the enhanced region. The vertical cross sections show that CO in the ASM region is enhanced throughout the troposphere up to the tropopause level. The enhancement in the UT is confined in the south by the tropical easterly jet and in the north by the subtropical westerly jet. The latitude-height cross section further shows the bulging tropopause structure at the center of the anticyclone. The tropopause is between 380 and 400 K θ in the monsoon region (10°–40°N). The relationship between the tropopause and the isentropes near the subtropical jet helps to understand the structure shown in Figure 1d that the region with higher tropopause θ is slightly shifted northward with respective to the region of higher tropopause height.

We further investigate the confinement of CO in the UT using the daily 100 hPa CO gradient across the "edge" of the anticyclone, defined by the maximum wind in this case, on four sides of the anticyclone. The result is given in Figure 3. We find that latitudinal CO distributions relative to the zonal wind maximum (Figures 3a and 3b) show a strong gradient across the edge of the anticyclone in the north-south directions. The 11 year

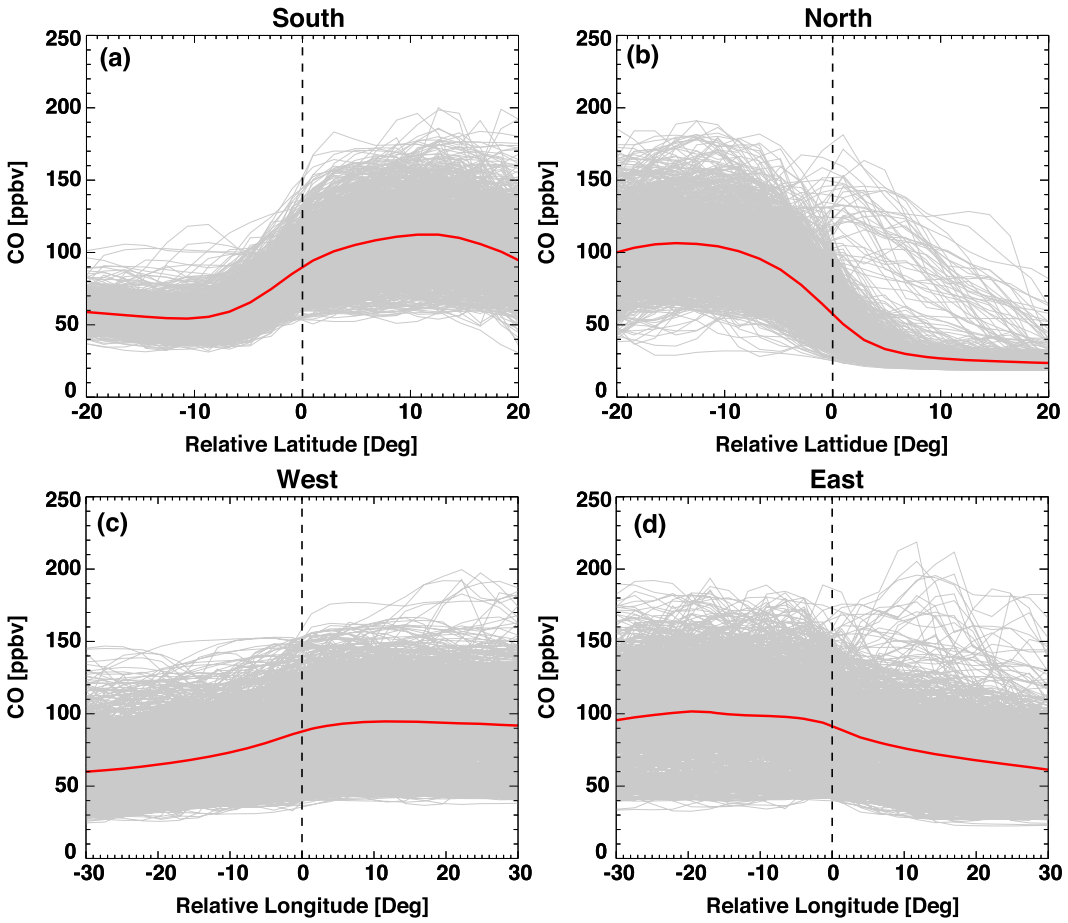

Figure 3. CO gradients across the maximum wind location on four sides of the anticyclone at the 100 hPa level. (a, b) In latitude relative to the position of maximum zonal wind. (c, d) In longitude relative to the position of maximum meridional wind. The thin gray lines show the daily CO mixing ratio (ppbv) along a south-north or east-west line across the maximum wind line on each side of the anticyclone. The red line represents the 11 year mean (average of all gray lines). The longitudinal location of the south-north lines is chosen as the maximum zonal wind location. The latitudinal position of the east-west lines is located by the zero zonal wind. Plots include all JJA days for the 11 years of WACCM4-SD run (2000–2010).

seasonal mean CO inside the anticyclone is higher than 100 ppbv, while it drops to around or below 50 ppbv outside the anticyclone. East-west gradients of CO are much weaker than their north-south counterparts; this is consistent with the weaker meridional winds and a reduced barrier to transport compared to zonal wind confinement in the north-south direction.

4. Tracers Under the Influence of Subseasonal-Scale Variability of the Anticyclone

The ASM upper tropospheric anticyclone can be considered as a stationary feature (Figure 1) only from the viewpoint of the seasonal time scale. Analysis of subseasonal variability reveals the prevalence of westward propagating waves. The general oscillatory behavior of the ASM has been observed in a number of monsoon elements, including the surface pressure of the monsoon trough and the Tibetan high, and it was examined in relation to the breaks in monsoon [*Krishnamurti and Bhalme*, 1976; *Krishnamurti and Ardanuy*, 1980]. In the upper troposphere, the transient behavior was seen as eddy shedding of the low potential vorticity (PV) air [*Hsu and Plumb*, 2000; *Popovic and Plumb*, 2001; *Garny and Randel*, 2013]. An analysis of the 100 hPa GPH shows that this transient behavior can be characterized as a bimodal oscillation between an eastern mode, also referred to as the Tibetan Plateau mode, and a western mode, or the Iranian Plateau mode [*Zhang et al.*, 2002]. An idealized simulation using a primitive equation model shows that the heating in the Tibetan plateau can create the low PV air at the upper troposphere, and the westward migration occurs as a result of instability

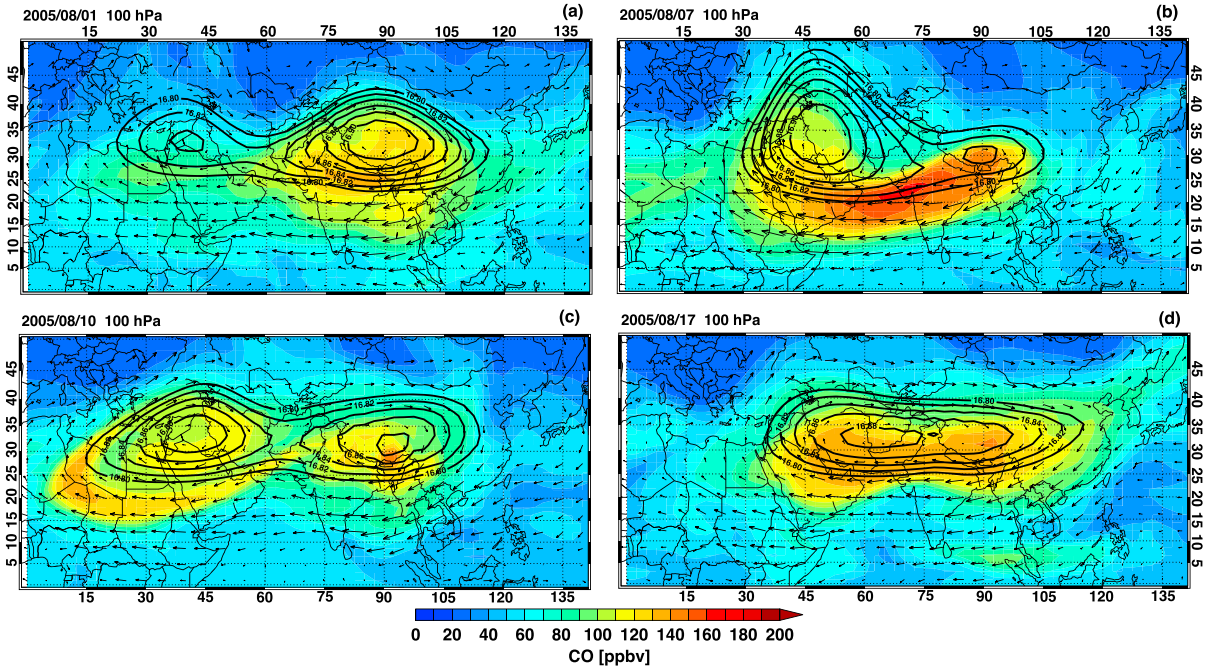

Figure 4. Subseasonal scale modulation of CO at 100 hPa associated with the bimodal oscillation of the anticyclone. The figure shows four selected days between 1 and 24 of August 2005; each represents a distinct phase of the anticyclone oscillation: (a) eastern (Tibetan plateau) phase, (b) western (Iranian plateau) phase, (c) double-center phase, and (d) longitudinally elongated phase. The WACCM CO field is shown in color shading. Dynamical variables are GPH (km; black contour) and horizontal wind (arrows) at the 100 hPa.

created by the low PV air in the background of higher PV on the southern and eastern flank of the anticyclone [*Liu et al*., 2007]. The bimodality and mechanisms that produce the phenomenon are topics of ongoing research [e.g., *Wu et al*., 2015; *Nützel et al*., 2016]. The goal of this work is not to explain the dynamics of bimodality for the anticyclone but rather to focus on the UTLS trace gas distribution and transport associated with the east-west oscillation.

The time period of 1–25 August 2005 is selected to illustrate the tracer behavior associated with the bimodal east-west oscillation. An animated view of this period for 100 hPa CO and associated dynamical fields is provided in the supporting information. Figure 4 shows CO concentrations from 4 days selected from this period to exemplify spatial patterns associated with four distinct phases of the bimodal oscillation of the anticyclone: (a) the eastern (or Tibetan plateau) phase, (b) the western (or the Iranian plateau) phase, (c) the double-center phase, and (d) the zonal elongated phase.

Figure 4 indicates that the CO field is transient and does not usually have the maximum enhancement in the center of the anticyclone. Rather, the oscillation appears to "stir" and mix the air with enhanced boundary layer tracer with the background UTLS. This behavior was also shown in analyses of CO and potential vorticity in *Garny and Randel* [2013].

To characterize the relationship between the variability of the circulation and the tracer field statistically, we examine the relationship between GPH and CO along the ridge of the anticyclone at the 150 hPa level. The 150 hPa level is chosen for this analysis because the level is a good representation of where the anticyclonic winds form a closed circulation. Figure 5 illustrates the ridge using the 150 hPa GPH on a selected day and identifies the study region. An example Hovmöller diagram of GPH and CO anomaly fields along the GPH ridgeline at 150 hPa for the JJA 2005 is given in Figure 6. In this example, the GPH anomaly field depicts the 10 to 20 day westward migration of the anticyclone, initiated from a persistent positive anomaly location near 80°–90°E, which can be associated with the eastern or the Tibetan Plateau mode. The western mode is not well defined as there does not appear to be a persistent positive anomaly at longitudes west of 70°E. The correlation coefficient between the CO and GPH anomaly fields in this example is 0.75 (determined from daily

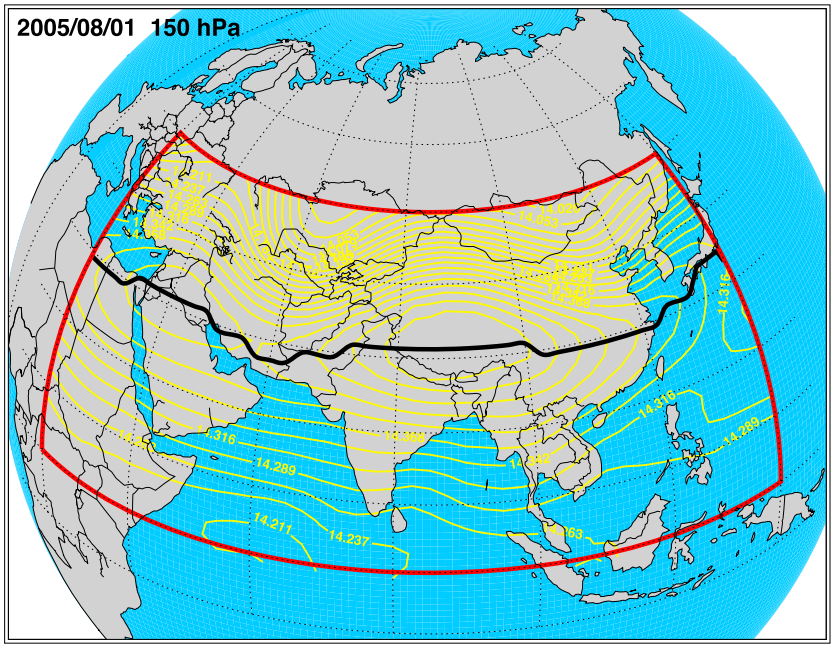

Figure 5. An example of the spatial extent of the anticyclone and the ridgeline using contours of GPH at the 150 hPa level on 1 August 2005. The red box shows the longitude (0°–140°E) range selected for the analysis of anomaly fields.

longitudinal variations for the entire 3 months). The most notable uncorrelated features are the frequent eastward "shedding," identified by the positive CO anomalies east of the region of GPH positive anomaly. The correlated behavior between the CO and the GPH suggests that the westward migration of the anticyclone might dictate the subseasonal-scale tracer field variability in the UTLS level. Although we have only shown examples from 2005 in this section, similar subseasonal-scale variability and correlated westward oscillations are seen in all 11 years of WACCM4-SD run.

Although not shown here, the similar east-west oscillation is found at levels throughout the depth of the anticyclone (200 hPa to 70 hPa). We have also examined the relation of 100 hPa CO anomaly and the tropopause anomaly and found similar correlative behavior in the subseasonal-scale east-west oscillation. Given that the CO enhancement at the tropopause level depends on multiple factors, including the surface emissions, convective uplifting, and the anticyclone confinement, the prevalent correlation suggests that the role of dynamical variability of the anticyclone is a significant driver for the distribution of UTLS CO in the model.

5. Is There a Preferred Pathway From BL to the Tropopause Level?

The question of the preferred pathway from the boundary layer to the tropopause level is relevant for identifying the most significant controlling mechanism for the uplifting and the most impactful source regions for the air mass transported into the UTLS. There has been a history of debate on whether convection over the Bay of Bengal or over the Tibetan plateau is the main contributor to the deep uplifting [*Fu et al*., 2006; *Park et al*., 2009]. Trajectory model analysis has led to the conclusion that most air masses in the anticyclone passed through a fairly narrow uplifting pathway [*Bergman et al*., 2013]. We expect the 3-D structure of the pollution tracer CO from WACCM4-SD to shed new light into this issue.

Figure 7 shows latitude-height cross section of CO across the center of the anticyclone (identified by the maximum GPH) for selected days, highlighting the difference in CO vertical structure between the eastern mode (Tibetan plateau) and the western mode (the Iranian plateau). The vertical uplifting of CO from the boundary layer to the tropopause level near the southern slope of the Tibetan plateau is apparent in the eastern mode (near 90°E) cross section, but only an upper tropospheric CO enhancement is seen in the cross section for the western mode (near 70°E in this case). This behavior is a robust feature of the WACCM4-SD run as demonstrated by Figures 7c and 7d. These figures show latitude-height cross sections of 11 year averaged CO

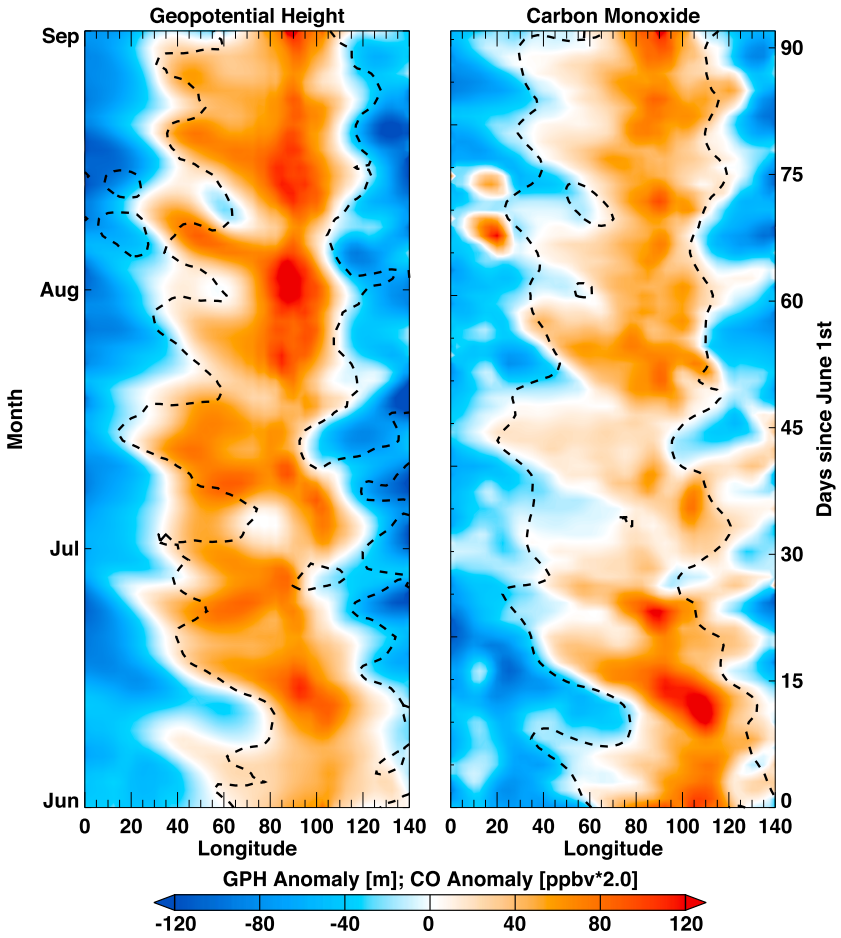

Figure 6. Hovmöller diagrams of 150 hPa GPH and CO anomalies along the GPH ridge line for JJA 2005. The anomaly fields are calculated with respect to the daily means along the GPH ridgeline. The dashed line in each panel indicates the location of the mean (zero anomaly) of the opposite field. In this specific case, the overall mean of GPH is 14,405 m, and CO mean is 131 ppbv. The Pearson's correlation of the two fields for the 3 months is 0.75.

anomalies (the Figure 7 caption defines these anomalies) along 90°E (the statistical center of the Tibetan mode; Figure 7c) [see *Zhang et al.*, 2002] and 60°E (Iranian mode; Figure 7d) during JJA and indicate that the relationship between upper tropospheric CO enhancement and a local lower tropospheric enhancement is a climatological feature of the Tibetan mode but not of the Iranian mode.

Figure 8 further identifies the preferred uplifting region using a plane view of CO enhancement throughout the troposphere. The figure shows the frequency of occurrence of CO $>$ 100 ppbv for every model level from the surface to 100 hPa, using 11 years of daily CO. The eastern mode of the anticyclone stands out as the only region of high frequency (50%–100%) of CO enhancement throughout the troposphere in the entire Northern Hemisphere for the season. Note this "deep tropospheric" enhancement pattern is not solely defined by surface emissions. Over the horizontal domain of Figure 8, there are three "hot spots" of high surface CO in the 11 year JJA mean of the model. These are over eastern China, northeastern India and part of Indonesia, with the eastern China being the largest area of intense CO emission (over 200 ppbv). The deep tropospheric hot spot shown in Figure 8 is therefore a compound effect of monsoon dynamics and the emission.

Multiple dynamical fields are overlaid in Figure 8 to provide the context for the deep tropospheric CO enhancement. The selected GPH and tropopause contours help identify the climatological mean location of the ASM anticyclone and the area of bulging tropopause. The southwesterly monsoonal flow is shown by the surface wind. The contours of low outgoing long-wave radiation (OLR $<$ 220 W/m^2) are shown as a proxy of persistent deep convection and clouds. Together, the figure suggests that persistent deep

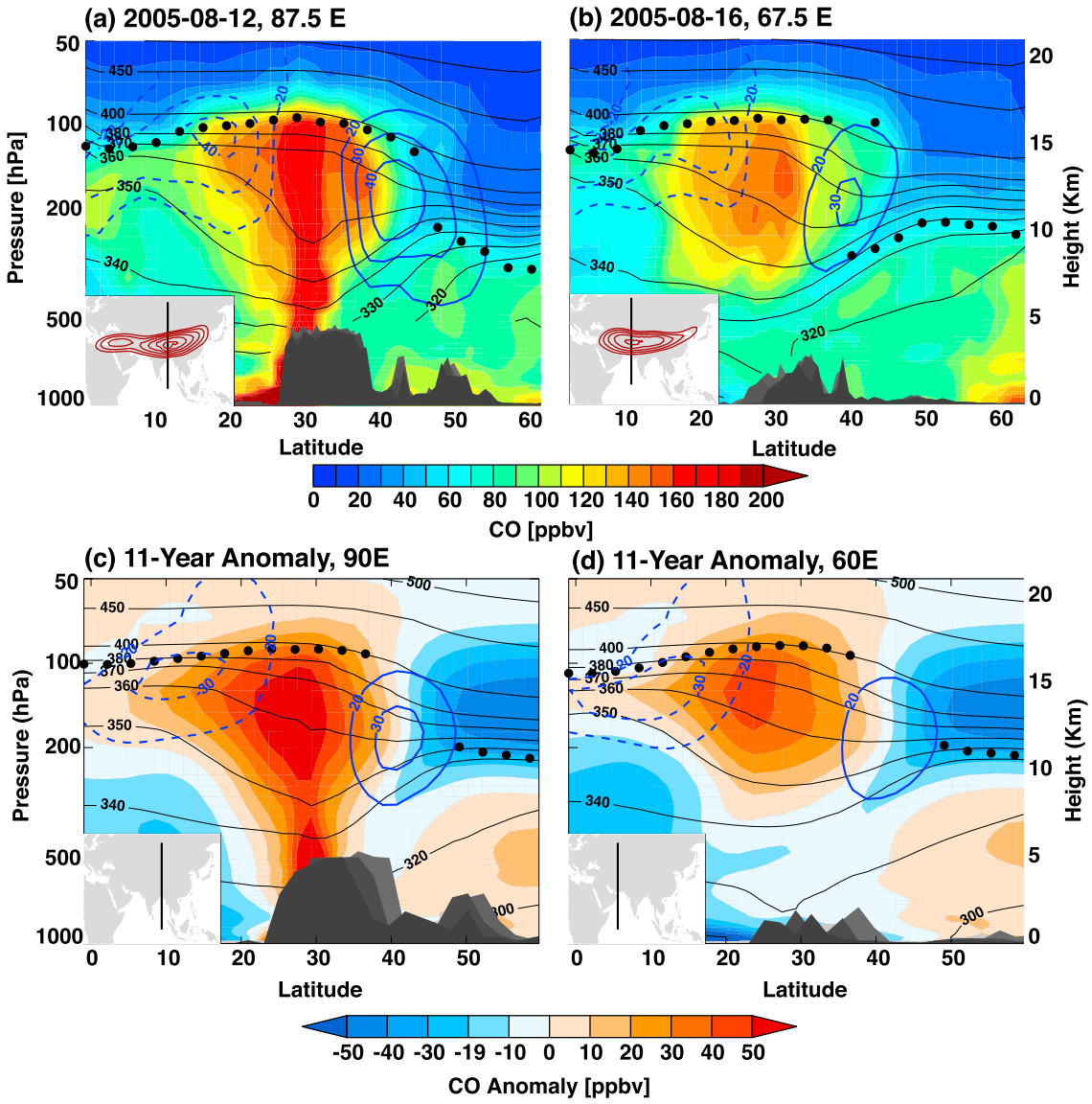

Figure 7. (a and b) WACCM CO mixing ratio latitude-pressure (altitude) cross sections for two selected longitudes and days representing the Tibetan (Figure 7a) and Iranian (Figure 7b) modes, respectively. (c and d) The 11 year mean of JJA daily CO anomaly, which is calculated with respect to the 11 year JJA mean vertical profile of CO for the box defined by 0–60°N latitude and 0–120°E longitude. The locator map of each cross section is shown at the lower left corner. Additional dynamical variables are the same as in Figure 2.

convection, the higher tropopause, and the surface flow that sweeps through highly polluted south Asia and reaches the convergence near the southern flank of the plateau are the key elements to the formation of the CO feature.

Note that the result shown in Figure 8 is very similar to Figure 7 of *Bergman et al.* [2013], where the trajectory model analysis showed a transport "conduit" feeding into the anticyclone. The location of the preferred Lagrangian pathway matches the location of the total column CO enhancement from the WACCM4-SD model. The Lagrangian model and WACCM4-SD therefore support each other on the location of preferred vertical transport from lower troposphere to the tropopause level. There is, however, a significant difference between the two analyses: the Lagrangian analysis was restricted to the parcels in the anticyclone at 100 hPa level, whereas the WACCM4-SD CO analyses applied to the entire domain with no reference to the anticyclone.

Figure 8 also complements the information in Figure 1d. Together, these analyses point to a scenario that the boundary layer air is primarily uplifted from in the southern edge of the Tibetan plateau, the region of

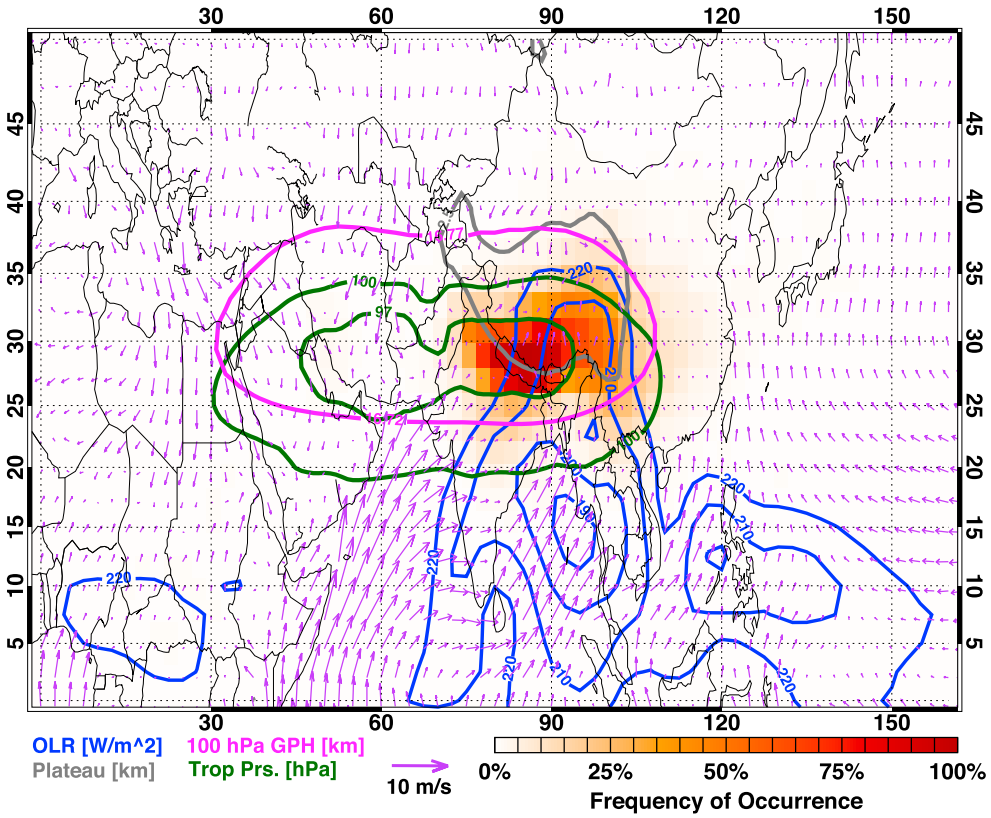

Figure 8. Frequency of occurrence of CO mixing ratio greater than 100 ppbv at every model pressure level from surface to 100 hPa for the 11 year WACCM4-SD run calculated from JJA daily data (total of 1012 days) (red shading). Also displayed are the climatological locations of the anticyclone, represented by the 16.72 km contour of 100 hPa GPH (magenta) and 100 hPa and 97 hPa tropopause pressure contour (green), and the outgoing long-wave radiation (OLR), representing the region of deep convection (blue contours). The location of the Tibetan Plateau is marked using the 2.5 km elevation using information from a digital elevation model data set (gray). The low-level flow pattern is indicated by the mean surface wind (purple arrows).

northern India, Nepal, and Southwestern China. In the UT, the westward migration on the 10 to 20 day time scale, together with the confinement of the anticyclone, fills the entire anticyclone with the CO enriched BL air. The 24 day evolution of the 100 hPa CO field given in the supporting information provides a clear example.

Dynamically, the tracer behavior is consistent with the large-scale flow pattern of an east-west cell, with a climatological ascending branch on the east over the Tibetan plateau and a descending branch on the west over the middle east [e.g., *Zhang et al*., 2002; *Wu et al*., 2015]. This circulation pattern is also described as a sustained dynamical coupling between the monsoon (east) and the desert (west) [*Rodwell and Hoskins*, 1996].

6. Relationship of ASM Uplifting With the Brewer-Dobson Circulation

Having demonstrated the effective role of ASM in pumping boundary layer air to the tropopause level, the questions remain on how the air mass in the tropospheric bubble enters the stratosphere, how directly does it occur, on what time scale, and what is the relationship of ASM chimney with the ascending branch of the Brewer-Dobson circulation (BDC). We investigate these questions using analyses of tracer vertical structures and vertical wind field on a seasonal time scale. For this study, we use a model tracer "E90" instead of CO. This is because the CO seasonal cycle is strongly influenced by seasonal changes of emissions. Although the CO UTLS structure leads to the same conclusion, the message is clearer using the E90 tracer.

The model tracer E90 is a global and homogeneously emitted boundary layer tracer with a 90 day decay lifetime [*Prather et al*., 2011]. The tracer was originally designed to identify the chemical tropopause, but it

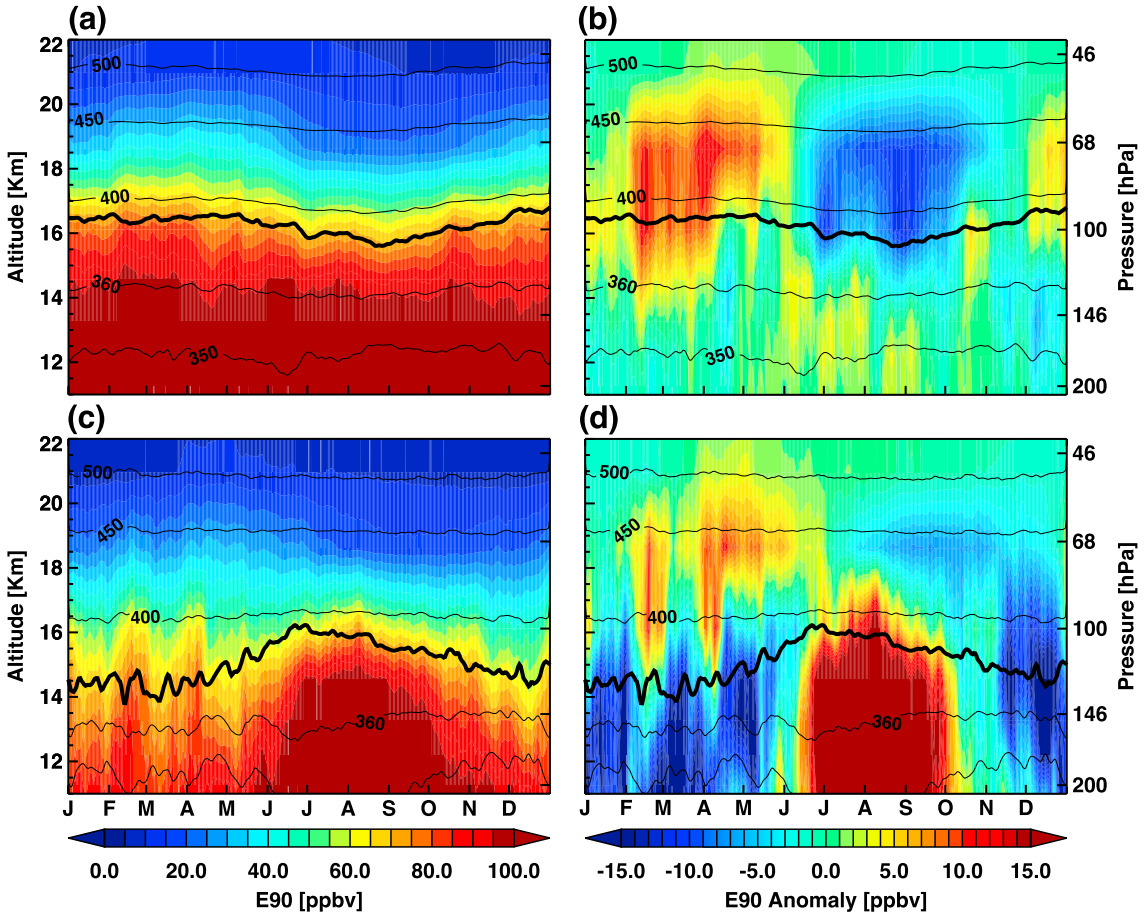

Figure 9. (a) Daily mean E90 tracer and (b) E90 anomaly at the UTLS levels (12–22 km) for the tropical belt (12°S– 12°N, 0°–360°E) for year 2014 from a multidecade WACCM4-SD run. (c) Same as Figure 9a but for the ASM box (15°–35°N, 0°–120°E). (d) Same as Figure 9b but for the ASM box. The anomaly profile is calculated each day (at each model pressure level) with respect to the annual mean profile in the corresponding belt or box. Also shown are tropopause height (thick black line) and selected isentropes (thin black lines).

also serves as a good medium-time-scale transport tracer. In many ways this tracer is similar to CO but without variations in surface source and seasonal change.

Figures 9 shows the seasonal changes of the vertical structure of E90 and E90 anomaly in the UTLS for the tropical belt and the ASM box. The anomaly profile is calculated each day with respect to the annual mean vertical profile in the corresponding belt or box. These figures show that, in the tropics, E90 has little seasonal variation in the UT and a strong annual variation in the lower stratosphere (LS) (as a response to seasonally varying tropical upwelling; similar behavior is observed for ozone and CO in the tropical LS, e.g., *Abalos et al*. [2012]). In the ASM box, monsoon vertical uplifting promotes a strong positive E90 anomaly in the upper troposphere. However, enhanced values of E90 stop close to the tropopause or ~400 K level. The tracer anomalies in the LS over the ASM are very similar to the tropics but with an approximate 1 month delay, consistent with the large influence of tropical lower stratosphere from isentropic transport and mixing.

Although not shown, we have done the same analysis using MLS and WACCM4-SD CO data. Apart from a more complicated seasonal pattern in the tropical upper troposphere, the tropopause level vertical structure is very similar to that of E90 shown in Figure 9.

To understand the apparent low efficiency of the vertical transport from the ASM anticyclone region into the stratosphere suggested by Figure 9, we complement the tracer analysis with the seasonal-scale structure of the vertical wind field. Figure 10 shows the seasonal mean vertical velocity, W (mm/s), as well as the latitude-month cross section of the Transformed Eulerian Mean (TEM) residual vertical velocity, W^* (mm/s) [see *Andrews et al*., 1987], for 0°–60°N latitude range at both 70 hPa and 100 hPa levels.

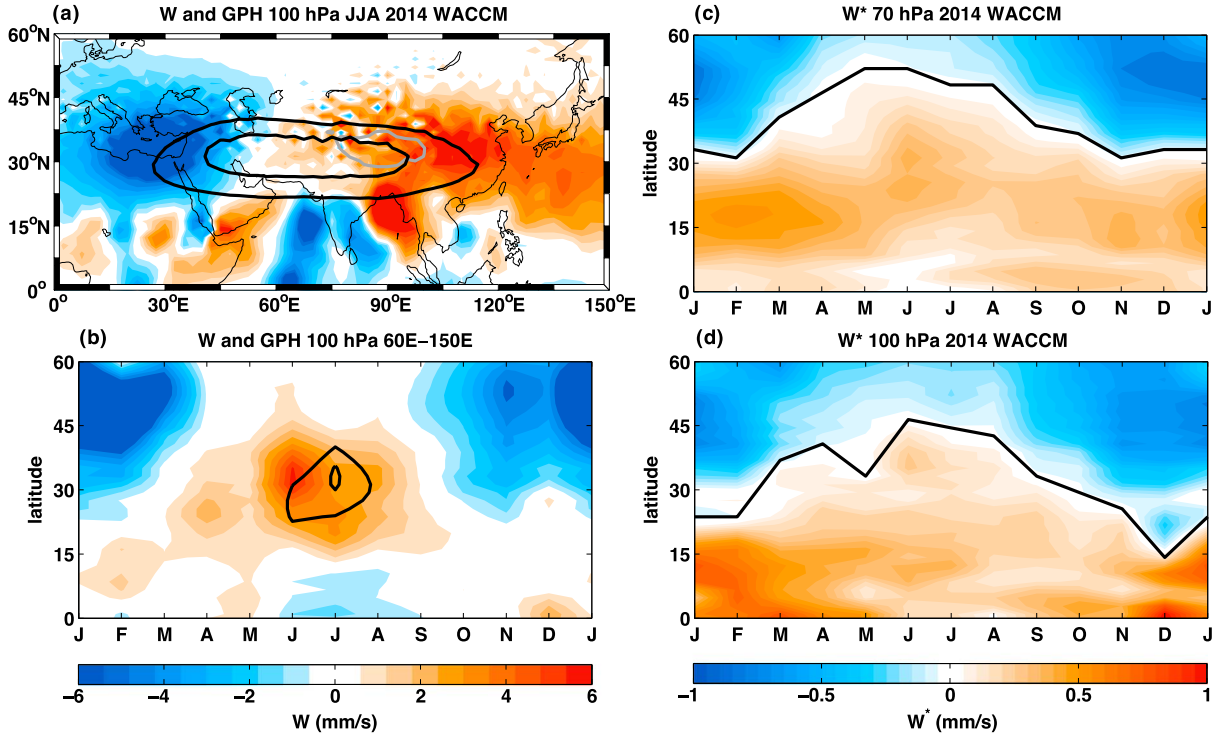

Figure 10. Vertical velocity (*W*) and the Transformed Eulerian Mean (TEM) residual circulation vertical velocity (*W**) at the UTLS level from WACCM4-SD for 2014. (a) Map of JJA seasonal mean *W* at 100 hPa level. (b) Latitude-month section of 100 hPa W for the eastern ASM longitude range (60°–150°E). The black contours in both Figures 10a and 10b show selected 100 hPa mean GPH (16.70 and 16.75 km) to indicate the location of the anticyclone. (c) and d) Latitude-month sections of the TEM vertical velocity (*W**) at 70 hPa and 100 hPa, respectively. In all cases, the ascending region is indicated by the warm color, descending region by the cold color.

The seasonal mean distribution of 100 hPa vertical wind (Figure 10a) shows a large-scale east-west circulation structure that ascends on the east side of the anticyclone and descends on the west side. This result agrees and complements a number of tropospheric circulation analyses of the region [e.g., *Rodwell and Hoskins*, 1996; *Zhang et al*., 2002]. This wind field pattern supports the contention that the east-west asymmetry of the CO anomaly in the anticyclone (Figures 7 and 8) is a result of a continental-scale circulation.

Figure 10b shows the monthly mean vertical velocity for 0°–60°N latitudes for the eastern side of Asian monsoon longitudinal segment (within 60–150°E). The figure shows a stronger seasonal northward migration of the ascending belt during the JJA season. The mean GPH field shows that the ASM anticyclone is located within the ascending circulation. This is consistent with the surface convergence and Intertropical Convergence Zone (ITCZ) analysis, which shows that there is a large seasonal migration in ITCZ location over the Indian Ocean sector, changing from ~10°S in Northern Hemisphere (NH) winter to ~ 30°N in NH summer, [*Lawrence and Lelieveld*, 2010]. A consistent message can also be drawn from Figure 8 that the convergence in the surface wind climatology is located directly beneath the center of the ASM anticyclone.

The zonal distribution of *W** (Figures 10c and 10d) shows that the residual circulation zero wind line, which marks the change from the ascending branch to the descending branch, has a strong seasonal cycle. It moves between 20°N (January) and 35° N (July) at 100 hPa, and shifts farther northward (by ~ 10°) at 70 hPa. These seasonal changes are consistent with the climatological analyses of *Eluszkiewicz et al*. [1996] and *Abalos et al*. [2015]. In addition to the change in the latitudinal location of the zero wind line, the figure also indicates that there is a seasonal cycle of the vertical ascent rate, with the strongest ascent in the December–February season and the weakest in JJA season. This change in vertical ascent strength and its effect on the seasonal cycles of tracers in lower stratosphere are well analyzed and discussed in numerous previous studies [e.g., *Randel et al*., 2008; *Abalos et al*., 2012]. The ASM is shown to be near the zero wind line in its latitude and during the weakest season of the stratospheric circulation.

The results shown in Figures 9 and 10 lead to a conclusion that, although the top of the ASM anticyclone is within the ascending branch of the Brewer-Dobson circulation, the weak rate of ascent in the ASM season

makes the ASM an ineffective pathway to transport air vertically into the deep stratosphere within the JJA season. The most effective transport from the ASM anticyclone is likely the quasi-isentropic eddy shedding and mixing at the level near 400 K [*Popovic and Plumb*, 2001; *Garny and Randel*, 2016]. The quasi-isentropic transport can lead to a fast (week to month) influence of air uplifted in the ASM in both the equatorial and the high-latitude lower stratosphere, eventually entering the ascending branch of the BDC, as indicated by HCN observations shown in *Randel et al*. [2010, Figure 2].

7. Conclusions and Discussions

We have investigated the relationship of boundary layer tracer transport and dynamical structures in the ASM using multiyear WACCM4-SD output. Using model CO and E90 tracers, we focus on the relationship of tracers and the dynamical structure of the ASM and a set of interrelated questions.

Our analysis shows that the ASM creates a bubble of tropospheric air above the global mean tropical tropopause of the season in both altitude and potential temperature coordinates. This concept is not entirely new and is partially indicated by previous studies [e.g., *Dethof et al*., 1999]. Our analysis using the relationship between model CO and tropopause highlights the chemical signature of the tropospheric bubble in the stratospheric background.

The higher potential temperature of the ASM tropopause allows the air in the bubble to isentropically shed into the overworld stratosphere (Figures 1 and 2) (typically considered for levels higher than 380 K; see *Hoskins* [1991]). The strong anticyclonic circulation confines this type of transport. Our analysis shows that the confinement is stronger in the north and south directions and weaker in the east and west directions. The air inside the bubble is therefore more likely to shed out from the east and west directions due to the weaker gradients in the winds.

While the model analysis presented here paints a consistent dynamical picture, it is important to note that neither this model analysis nor previous satellite data analyses [e.g., *Park et al*., 2007; *Randel et al*., 2010] have sufficient spatial and time resolution to accurately characterize the transport processes associated with the ASM anticyclone. In particular, in situ observations of the chemical and dynamical variables in the ASM UTLS region are important for confidently interpreting the dynamical structure of the bubble and its impact on transport.

The model CO structure indicates that there is a preferred location of vertical transport. The uplifting of boundary layer pollutants to the tropopause level occurs primarily on the eastern side of the anticyclone, centered near the southern flank of the Tibetan Plateau, northeast India and Nepal, and north of the Bay of Bengal. This conclusion is consistent with the conclusion of a Lagrangian model study, where a conduit connecting the boundary layer air into the anticyclone is found [*Bergman et al*., 2013].

Our analysis also shows that the subseasonal-scale east-west oscillation of the anticyclone plays a significant role in the variability and transport of boundary layer tracers at the UTLS level. The westward propagation of the anticyclone serves to transport the uplifted boundary layer air westward and fill the entire anticyclone with the boundary layer air. This westward transport associated with the migration of the anticyclone from the Tibetan plateau mode to the Iranian plateau mode is consistent with previous analyses using low PV air [*Popovic and Plumb*, 2001; *Garny and Randel*, 2013].

Using the model E90 tracer, we find that the seasonal evolution of the positive anomaly signature of the boundary layer tracer in the ASM region falls off sharply at the 400 K level. The model result therefore suggests that although the ASM uplifting connects directly with the BDC ascending branch in the stratosphere, the boreal summer minimum in BDC vertical motion makes the vertical transport of ASM air mass into the deep stratosphere inefficient. Quasi-isentropic transport, often in the form of eddy shedding in the east-west direction, is likely the primary mode for the uplifted air to enter the stratosphere. The isentropic transport is found to have rapid influence to both equatorial and high latitudes [*Garny and Randel*, 2016], which allows continued ascent into the deep stratosphere via the BDC ascending branch (i.e., the "tropical pipe").

The model analysis overall indicates that the ASM transport in the process of uplifting from the boundary layer to the tropopause level behaves like a chimney, dominated by the stationery, localized venting (e.g., Figure 8). This behavior changes at the UT level, and the transport in becomes more like an "oscillatory

blower" (e.g., Figure 4 and the animation in the supporting information), influenced by the east-west oscillation of the anticyclone.

Lastly, we want to emphasize the potential limitations of the model representation used here. Representing convection and the convective-driven dynamical conditions is a significant challenge for global models of this type. The results of the model analysis presented in this work should therefore be considered as hypotheses to be tested with field observations; in particular with airborne studies that examine the chemical gradients, both vertically and horizontally across the tropopause, and address the questions of how the ASM impacts the lower stratosphere, the deep stratosphere, and possibly the chemistry of the polar region. In situ measurements of the chemical content within and outside of the anticyclone, especially of shorter-lived species, will provide the information necessary for evaluating the model representation of convective transport. Measurements of chemically active species in the core and the outflow of the anticyclone are also essential for quantifying the impact of monsoon convection over polluted regions on chemistry and ozone production in the UTLS.

Acknowledgments
The National Center for Atmospheric Research is operated by the University Corporation for Atmospheric Research under sponsorship of the National Science Foundation. WACCM is a component of NCAR's Community Earth System Model (CESM), which is supported by the National Science Foundation (NSF) and the Office of Science of the U.S. Department of Energy. Computing resources were provided by NCAR's Climate Simulation Laboratory, sponsored by NSF and other agencies. This research was enabled by the computational and storage resources of NCAR's Computational and Informational Systems Laboratory (CISL).

References

Abalos, M., W. J. Randel, and E. Serrano (2012), Variability in upwelling across the tropical tropopause and correlations with tracers in the lower stratosphere, *Atmos. Chem. Phys.*, *12*, 11,505–11,517, doi:10.5194/acp-12-11505-2012.

Abalos, M., B. Legras, F. Ploeger, and W. J. Randel (2015), Evaluating the advective Brewer-Dobson circulation in three reanalyses for the period 1979–2012, *J. Geophys. Res. Atmos.*, *120*, 7534–7554, doi:10.1002/2015JD023182.

Andrews, D. G., J. R. Holton, and C. B. Leovy (1987), *Middle Atmosphere Dynamics*, 489 pp., Elsevier, New York.

Bergman, J. W., F. Fierli, E. J. Jensen, S. Honomichl, and L. L. Pan (2013), Boundary layer sources for the Asian anticyclone: Regional contributions to a vertical conduit, *J. Geophys. Res. Atmos.*, *118*, 2560–2575, doi:10.1002/jgrd.50142.

Chen, B., X. D. Xu, S. Yang, and T. L. Zhao (2012), Climatological perspectives of air transport from atmospheric boundary layer to tropopause layer over Asian monsoon regions during boreal summer inferred from Lagrangian approach, *Atmos. Chem. Phys.*, *12*, 5827–5839.

Dethof, A., A. O'Neill, J. M. Slingo, and H. G. J. Smit (1999), A mechanism for moistening the lower stratosphere involving the Asian summer monsoon, *Q. J. R. Meteorol. Soc.*, *125*, 1079–1106.

Eluszkiewicz, J., et al. (1996), Residual circulation in the stratosphere and lower mesosphere as diagnosed from Microwave Limb Sounder data, *J. Atmos. Sci.*, *53*, 217–240.

Emmons, L. K., et al. (2010), Description and evaluation of the Model for Ozone and Related chemical Tracers, version 4 (MOZART-4), *Geosci. Model Dev.*, *3*, 43–67, doi:10.5194/gmd-3-43-2010.

Fu, R., Y. Hu, J. S. Wright, J. H. Jiang, R. E. Dickinson, M. Chen, M. Filipiak, W. G. Read, J. W. Waters, and D. L. Wu (2006), Short circuit of water vapor and polluted air to the global stratosphere by convective transport over the Tibetan Plateau, *Proc. Natl. Acad. Sci. U.S.A.*, *103*, 5664–5669, doi:10.1073/pnas.0601584103.

Garny, H., and W. J. Randel (2013), Dynamic variability of the Asian monsoon anticyclone observed in potential vorticity and correlations with tracer distributions, *J. Geophys. Res. Atmos.*, *118*, 13,421–13,433, doi:10.1002/2013JD020908.

Garny, H., and W. J. Randel (2016), Transport pathways from the Asian monsoon anticyclone to the stratosphere, *Atmos. Chem. Phys.*, *16*, 2703–2718, doi:10.5194/acp-16-2703-2016.

Granier, C., J. F. Lamarque, A. Mieville, J. F. Muller, J. Olivier, J. Orlando, J. Peters, G. Petron, G. Tyndall, S. Wallens (2005), POET, a database of surface emissions of ozone precursors. [http://www.aero.jussieu.fr/projet/ACCENT/POET.php.]

Hack, J. J. (1994), Parameterization of moist convection in the National Center for Atmospheric Research community climate model (CCM2), *J. Geophys. Res.*, *99*(D3), 5,551–5,568, doi:10.1029/93JD03478.

Highwood, E. J., and B. J. Hoskins (1998), The tropical tropopause, *Q. J. R. Meteorol. Soc.*, *124*, 1579–1604.

Hoskins, B. J. (1991), Towards a PV-θ view of the general circulation, *Tellus*, *43AB*, 27–35.

Hoskins, B. J., and M. J. Rodwell (1995), A model of the Asian summer monsoon: I—The global scale, *J. Atmos. Sci.*, *52*, 1329–1340.

Hoskins, B. J., M. E. McIntyre, and A. W. Robertson (1985), On the use and significance of isentropic potential vorticity maps, *Q. J. R. Meteorol. Soc.*, *111*, 877–946.

Hsu, C. J., and R. A. Plumb (2000), Nonaxisymmetric thermally driven circulations and upper-tropospheric monsoon dynamics, *J. Atmos. Sci.*, *57*, 1255–1276.

Kinnison, D. E., et al. (2007), Sensitivity of chemical tracers to meteorological parameters in the MOZART-3 chemical transport model, *J. Geophys. Res.*, *112*, D20302, doi:10.1029/2006JD007879.

Krishnamurti, T. N., and H. H. Bhalme (1976), Oscillations of a monsoon system: I—Observational aspects, *J. Atmos. Sci.*, *33*, 1937–1954.

Krishnamurti, T. N., and P. Ardanuy (1980), The 10 to 20-day westward propagating mode and "Breaks in the Monsoons", *Tellus*, *32*, 15–26.

Kunz, A., L. L. Pan, P. Konopka, D. E. Kinnison, and S. Tilmes (2011), Chemical and dynamical discontinuity at the extratropical tropopause based on START08 and WACCM analyses, *J. Geophys. Res.*, *116*, D24302, doi:10.1029/2011JD016686.

Lamarque, J.-F., et al. (2012), CAM-chem: Description and evaluation of interactive atmospheric chemistry in CESM, *Geosci. Model Dev.*, *5*, 369–411, doi:10.5194/gmd-5-369-2012.

Lawrence, M. G., and J. Lelieveld (2010), Atmospheric pollutant outflow from southern Asia: A review, *Atmos. Chem. Phys.*, *10*, 11,017–11,096, doi:10.5194/acp-10-11017-2010.

Liu, Y. M., B. J. Hoskins, and M. Blackburn (2007), Impact of Tibetan orography and heating on the summer flow over Asia, *J. Meteorol. Soc. Jpn.*, *85B*, 1–19.

Lin, S.-J. (2004), A "vertically-Lagrangian" finite-volume dynamical core for global atmospheric models, *Mon. Wea. Rev.*, *132*, 2293–2307.

Marsh, D. R., M. J. Mills, D. E. Kinnison, J. F. Lamarque, N. Calvo, and L. M. Polvani (2013), Climate change from 1850 to 2005 simulated in CESM1(WACCM), *J. Clim.*, *26*, 7372–7391, doi:10.1175/jcli-D-12-00558.1.

Munchak, L. A., and L. L. Pan (2014), Separation of the lapse rate and the cold point tropopauses in the tropics and the resulting impact on cloud top-tropopause relationships, *J. Geophys. Res. Atmos.*, *119*, 7963–7978, doi:10.1002/2013JD021189.

National Centers for Environmental Prediction/National Weather Service/NOAA/U.S. Department of Commerce (2000), NCEP FNL operational model global tropospheric analyses continuing from July 1999. [Available at 10.5065/D6M043C6Research Data Archive at the National Center for Atmospheric Research, Computational and Information Systems Laboratory, Boulder, Colo.]

Neale, R., J. Richter, S. Park, P. Lauritzen, S. Vavrus, P. Rasch, and M. Zhang (2013), The mean climate of the Community Atmosphere Model (CAM4) in forced SST and fully coupled experiments, *J. Clim.*, *26*, 5150–5168.

Nützel, M., M. Dameris, and H. Garny (2016), Is there bimodality of the South Asian High?, *Atmos. Chem. Phys. Discuss.*, doi:10.5194/acp-2016-362, in review.

Olivier, J., J. Peters, C. Granier, G. Petron, J. Muller, and S. Wallens (2003), Present and future surface emissions of atmospheric compounds, POET report #2, EU project EVK2-1999-00011, [Available at http://www.aero.jussieu.fr/projet/ACCENT/POET. Php.]

Park, M., W. J. Randel, A. Gettelman, S. T. Massie, and J. H. Jiang (2007), Transport above the Asian summer monsoon anticyclone inferred from Aura Microwave Limb Sounder tracers, *J. Geophys. Res.*, *112*, D16309, doi:10.1029/2006JD008294.

Park, M., W. J. Randel, L. Emmons, P. Bernath, K. Walker, and C. Boone (2008), Chemical isolation of the Asian monsoon anticyclone observed in Atmospheric Chemistry Experiment (ACE-FTS) data, *Atmos. Chem. Phys.*, *8*, 757–764.

Park, M., W. J. Randel, L. K. Emmons, and N. J. Livesey (2009), Transport pathways of carbon monoxide in the Asian summer monsoon diagnosed from Model of Ozone and Related Tracers (MOZART), *J. Geophys. Res.*, *114*, D08303, doi:10.1029/2008JD010621.

Park, M., W. J. Randel, D. E. Kinnison, L. K. Emmons, P. F. Bernath, K. A. Walker, C. D. Boone, and N. J. Livesey (2013), Hydrocarbons in the upper troposphere and lower stratosphere observed from ACE-FTS and comparisons with WACCM, *J. Geophys. Res. Atmos.*, *118*, 1964–1980, doi:10.1029/2012JD018327.

Popovic, J. M., and R. A. Plumb (2001), Eddy shedding from the upper tropospheric Asian monsoon anticyclone, *J. Atmos. Sci.*, *58*, 93–104.

Prather, M. J., X. Zhu, Q. Tang, J. Hsu, and J. L. Neu (2011), An atmospheric chemist in search of the tropopause, *J. Geophys. Res.*, *116*, D04306, doi:10.1029/2010JD014939.

Randel, W. J., and M. Park (2006), Deep convective influence on the Asian summer monsoon anticyclone and associated tracer variability observed with Atmospheric Infrared Sounder (AIRS), *J. Geophys. Res.*, *111*, D12314, doi:10.1029/2005JD006490.

Randel, W. J., R. R. Garcia, and F. Wu (2008), Dynamical balances and tropical stratospheric upwelling, *J. Atmos. Sci.*, *65*, 3584–3595.

Randel, W. J., M. Park, L. Emmons, D. Kinnison, P. Bernath, K. A. Walker, C. Boone, and H. Pumphrey (2010), Asian monsoon transport of pollution to the stratosphere, 31, *Science*, *328*, 611–613, doi:10.1126/science.1182274.

Rienecker, M. M., et al. (2008), The GEOS-5 data assimilation system—Documentation of versions 5.0.1, 5.1.0, and 5.2.0, NASA Technical Report Series on Global Modeling and Data Assimilation, V27, NASA/TM-2008-104606.

Rodwell, M. J., and B. I. Hoskins (1996), Monsoons and the dynamics of deserts, *Q. J. R. Meteorol. Soc.*, *122*, 1385–1404.

Thomason, L. W., and J.-P. Vernier (2013), Improved SAGE II cloud/aerosol categorization and observations of the Asian tropopause aerosol layer: 1989–2005, *Atmos. Chem. Phys.*, *13*, 4605–4616, doi:10.5194/acp-13-4605-2013.

van der Werf, G. R., Randerson, J. T., Giglio, L., Collatz, G. J., Kasibhatla, P. S., and Arellano Jr., A. F. (2006), Interannual variability in global biomass burning emissions from 1997 to 2004, *Atmos. Chem. Phys.*, *6*, 3423–3441. [http://www.atmos-chem-phys.net/6/3423/2006/.]

Vernier, J.-P., L. W. Thomason, and J. Kar (2011), CALIPSO detection of an Asian tropopause aerosol layer, *Geophys. Res. Lett.*, *38*, L07804, doi:10.1029/2010GL046614.

Vernier, J.-P., T. D. Fairlie, M. Natarajan, F. G. Wienhold, J. Bian, B. G. Martinsson, S. Crumeyrolle, L. W. Thomason, and K. Bedka (2015), Increase in upper tropospheric and lower stratospheric aerosol levels and its potential connection with Asian pollution, *J. Geophys. Res. Atmos.*, *120*, 1608–1619, doi:10.1002/2014JD022372.

Vogel, B., G. Günther, R. Müller, J.-U. Grooß, and M. Riese (2015), Impact of different Asian source regions on the composition of the Asian monsoon anticyclone and of the extratropical lowermost stratosphere, *Atmos. Chem. Phys.*, *15*, 13,699–13,716, doi:10.5194/acp-15-13699-2015.

World Meteorological Organization (1957), Meteorology—A three-dimensional science: Second session of the commission for aerology, *World Meteorol. Organ. Bull.*, *4*, 134–138.

Wu, G. X., B. He, Y. M. Liu, Q. Bao, and R. C. Ren (2015), Location and variation of the summertime upper-troposphere temperature maximum over South Asia, *Clim. Dyn.*, *5*, 2757–2774, doi:10.1007/s00382-015-2506-4.

Yu, P., O. B. Toon, R. R. Neely, B. G. Martinsson, and C. A. M. Brenninkmeijer (2015), Composition and physical properties of the Asian tropopause aerosol layer and the North American tropospheric aerosol layer, *Geophys. Res. Lett.*, *42*, 2540–2546, doi:10.1002/2015GL063181.

Zhang, G. J., and N. A. McFarlane (1995), Sensitivity of climate simulations to the parameterization of cumulus convection in the Canadian Climate Centre general circulation model, *Atmos. Ocean*, *33*(3), 407–446.

Zhang, Q., G. X. Wu, and Y. F. Qian (2002), The bimodality of the 100 hPa South Asia high and its relationship to the climate anomaly over East Asia in summer, *J. Meteorol. Soc. Jpn.*, *80*, 733–744.